

Adsorption-controlled growth of La-doped BaSnO₃ by molecular-beam epitaxy

Hanjong Paik,¹ Zhen Chen,² Edward Lochocki,³ Ariel Seidner H.,¹ Amit Verma,⁴ Nicholas Tanen,^{1,5} Jisung Park,¹ Masaki Uchida,⁶ ShunLi Shang,⁷ Bi-Cheng Zhou,⁷ Mario Brützm,⁸ Reinhard Uecker,⁸ Zi-Kui Liu,⁷ Debdeep Jena,^{1,5} Kyle M. Shen,^{3,9} David A. Muller,^{2,9} and Darrell G. Schlom^{1,9,a}

¹ Department of Material Science and Engineering, Cornell University, Ithaca, New York 14853, USA

² School of Applied and Engineering Physics, Cornell University, Ithaca, New York 14853, USA

³ Laboratory of Atomic and Solid State Physics, Department of Physics, Cornell University, Ithaca, New York 14853, USA

⁴ Department of Electrical Engineering, IIT Kanpur, Kanpur 208016, India

⁵ School of Electrical and Computer Engineering, Cornell University, Ithaca, New York 14853, USA

⁶ Department of Applied Physics and Quantum-Phase Electronics Center (QPEC), University of Tokyo, Tokyo 113-8656, Japan

⁷ Department of Materials Science and Engineering, The Pennsylvania State University, University Park, Pennsylvania 16802, USA

⁸ Leibniz Institute for Crystal Growth, D-12489 Berlin, Germany

⁹ Kavli Institute at Cornell for Nanoscale Science, Ithaca, New York 14853, USA

^a Author to whom correspondence should be addressed. Electronic address: schlom@cornell.edu

Abstract

Epitaxial La-doped BaSnO₃ films were grown in an adsorption-controlled regime by molecular-beam epitaxy, where the excess volatile SnO_x desorbs from the film surface. A film grown on a (001) DyScO₃ substrate exhibited a mobility of 183 cm²·V⁻¹·s⁻¹ at room temperature and 400 cm²·V⁻¹·s⁻¹ at 10 K, despite the high concentration (1.2×10¹¹ cm⁻²) of threading dislocations present. In comparison to other reports, we observe a much lower concentration of (BaO)₂ Ruddlesden-Popper crystallographic shear faults. This suggests that in addition to threading dislocations that other defects—possibly (BaO)₂ crystallographic shear defects or point defects—significantly reduce the electron mobility.

Transparent conducting oxides with high mobility are being studied in hopes of realizing high-performance transparent electronics.¹ La-doped BaSnO₃ has emerged as a material of interest in this arena due to its high mobility at room temperature, transparency, and stability. La-doped BaSnO₃ single crystals are reported to have mobilities as high as 320 cm²·V⁻¹·s⁻¹ at room temperature at a mobile electron concentration of $n=8\times 10^{19}$ cm⁻³.² Indeed, La-doped BaSnO₃ has a higher mobility than all mainstream semiconductors (Si, GaAs, GaN, etc.) at doping concentrations above about $n=10^{19}$ cm⁻³, where it is degenerately doped;³ CdO is the only transparent semiconductor with higher mobility in this doping range.⁴ Another advantage of BaSnO₃ is its excellent structural match to ferroelectric and antiferroelectric oxides with the perovskite structure, e.g., Pb(Zr,Ti)O₃. This could enable La-doped BaSnO₃ to serve as a high mobility channel for smart transistors⁵ including ferroelectric field-effect transistors⁶⁻¹⁶ and yield a subthreshold slope beating the 60 mV/decade Boltzmann limit of conventional field-effect transistors by fabricating negative capacitance field-effect transistors (NCFET).^{17,18}

Two major deficiencies of today's epitaxially grown La-doped BaSnO₃ films that impact the performance of field-effect devices are (1) their mobility is significantly lower^{2,3,19-24} than what has been demonstrated in La-doped BaSnO₃ single crystals^{2,24,25} and (2) when doped below about 1×10^{19} cm⁻³ they are no longer conductive.^{2,3,19-24} This latter point also applies to La-doped BaSnO₃ single crystals.^{2,24} Both of these issues relate to the presence of significant concentrations of defects. The low mobility has been attributed to the high density of threading dislocations in epitaxial BaSnO₃ films that arise because they are grown on substrates to which they are poorly lattice matched.^{2,19-24} High concentrations of threading dislocations are known to limit the mobility of other semiconductors including Ge,²⁶ (In,Ga)As,²⁷ In(As,Sb),²⁸ SiGe,²⁹ and GaN.³⁰ Indeed the mobilities of epitaxial GaN and BaSnO₃ films with threading dislocation

densities in the 10^{10} – 10^{11} cm^{-2} range have been observed to scale with the square root of the mobile carrier concentration,^{2,19,30} in agreement with theory.^{26,30} In addition to the ability of dislocations to trap charge, nonstoichiometry, i.e., the ratio of (La+Ba):Sn deviating from 1 in La-doped BaSnO_3 films and the point defects it leads to, could also be responsible for the insulating behavior seen in lightly La-doped BaSnO_3 thin films. The inability to lightly dope La-doped BaSnO_3 layers is an obstacle to the fabrication of depletion-mode field-effect transistors.

The cutoff at about 1×10^{19} cm^{-3} in mobile electron concentration, below which doped films are insulating, is indicative of the concentration of electron traps in BaSnO_3 thin films. If nonstoichiometry is the root of the traps, then insulating behavior below a lanthanum concentration of 1×10^{19} cm^{-3} implies that the films deviate by 0.07% or more from being stoichiometric. This value is comparable to state-of-the-art stoichiometry control in the deposition of multicomponent films by physical vapor deposition methods.³¹⁻³⁹ A way to circumvent this limit is to exploit thermodynamics by entering an adsorption-controlled growth regime where the volatile constituents are provided in excess, but film composition is controlled automatically and locally through the volatility of those constituents to produce single-phase films.⁴⁰⁻⁴⁹ Adsorption-control has been extensively used for the growth of oxides⁵⁰⁻⁵² including, most recently, for the growth of epitaxial BaSnO_3 films utilizing metalorganic precursors.⁵³

In this Letter, we utilize adsorption-controlled growth with inorganic precursors to achieve La-doped BaSnO_3 thin films with (1) higher mobility and (2) that are conductive to lower carrier concentrations than have been reported to date. Room-temperature mobilities in excess of $150 \text{ cm}^2 \cdot \text{V}^{-1} \cdot \text{s}^{-1}$, the prior mobility record,²² are achieved in fully relaxed La-doped BaSnO_3 thin films on substrates with mismatches ranging from -5.1% (SrTiO_3) to -2.3% (PrScO_3). Our result

demonstrates that dislocations are not the only defect that limit the mobility in La-doped BaSnO₃ thin films and emphasizes the importance of precisely controlling film stoichiometry.

La-doped BaSnO₃ thin films were grown in a Veeco GEN10 MBE system from molecular beams emanating from separate effusion cells containing lanthanum (99.996% purity, Ames Lab), barium (99.99% purity, Sigma-Aldrich), and SnO₂ (99.996% purity, Alfa Aesar), respectively, in combination with a molecular beam of oxidant (the ~10% ozone + oxygen output of a commercial ozone generator).⁵⁴ The fluxes emanating from the effusion cells were determined by a quartz crystal microbalance (QCM) before growth. To achieve the desired doping concentration, the lanthanum flux was adjusted from the temperature at which its flux was measured by the QCM to a lower temperature, where accurate QCM measurements are not possible, by extrapolating its flux using the known activation energy of the vapor pressure of lanthanum,⁵⁵ i.e., a linear extrapolation of a plot of lanthanum vapor pressure vs. $1/T$. According to vapor pressure calculations, multiple species evaporate from SnO₂ under our growth conditions, with the major species being SnO.⁵⁶ In the supplementary material (S1) the calculated vapor pressure of species over solid SnO₂ are plotted at a fixed oxygen partial pressure of 7.6×10^{-7} Torr (10^{-9} atm). We used an excess of SnO_x-flux (above 9.0×10^{13} atoms·cm⁻²·s⁻¹) during growth, which is approximately three times greater than the barium flux (3.0×10^{13} atoms·cm⁻²·s⁻¹). The background pressure of the oxidant, 10% O₃ + O₂, was held at a constant ion gauge pressure of 7.0×10^{-7} Torr. All components—lanthanum, barium, SnO_x, and the 10% O₃ + O₂ oxidant—were co-supplied during film growth. A variety of perovskites substrates were used: (100) SrTiO₃, (001) DyScO₃, (110) DyScO₃, (110) TbScO₃, (110) GdScO₃, (110) Nd_{0.5}Sm_{0.5}ScO₃, (110) NdScO₃, and (110) PrScO₃.⁵⁷ These are all pseudocubic perovskite {100} surfaces and upon them the BaSnO₃ films grew with a cube-on-(pseudo)cube orientation

relationship. The substrate temperature was maintained between 830-850 °C, as measured by an optical pyrometer. To determine the optimal single-phase growth window, we used *in situ* reflection high-energy electron diffraction (RHEED) as described below. The RHEED intensity oscillation period was used to estimate the film thickness and growth rate. The film growth rate was about 0.3 Å/s.

The phase purity and structural perfection of the films were assessed using four-circle x-ray diffraction (XRD) utilizing Cu K_α radiation with a high-resolution diffractometer (Panalytical X'Pert Pro MRD with a PreFix hybrid 4×Ge 220 monochromator on the incident beam side and a triple axis/rocking curve attachment (Ge 220) on the diffracted beam side). The microstructure and defects in the film were studied by cross-sectional and plan-view high (low)-angle annular dark field scanning transmission electron microscopy (HAADF-STEM and LAADF-STEM) with an FEI Titan Themis with a probe aberration corrector at 300 kV. Temperature-dependent electrical transport and Hall effect were measured in a van der Pauw geometry with contacts made by wire bonding.

Figure 1 shows the calculated oxygen partial pressure (P_{O_2}) vs. temperature (T) diagram for the Ba-Sn-O system with the tin partial pressure fixed at 7.6×10^{-8} Torr (10^{-10} atm). It is constructed using the CALPHAD method and first-principles calculations (see supplementary material for additional details (S2)).⁵⁸ The reaction enthalpy (ΔH) values shown in Table I are used for the formation of $Ba_{n+1}Sn_nO_{3n+1}$ phases with $n=1, 2, 3,$ and 4 . The result is the four regions of stable solid phases shown in Fig. 1: **(I)** BaO, **(II)** Ba_2SnO_4 , **(III)** $BaSnO_3$, and **(IV)** SnO_2 , where the volatile SnO_x gas phases are balanced with each solid phase. First-principles calculations indicate that there is no driving force to form $Ba_{n+1}Sn_nO_{3n+1}$ with $n > 2$;⁵⁹ hence the phases of $Ba_{n+1}Sn_nO_{3n+1}$ with $n > 2$ are not shown in Fig. 1; they are all lumped into stability

region **II**. Overlaid onto Fig. 1 are RHEED patterns of La-doped BaSnO₃ thin films grown on (001) DyScO₃ substrates at different growth conditions (oxidant pressure and temperature).

Within region **III** stoichiometric BaSnO₃ films grow free of any surface reconstruction, i.e., with a 1×1 RHEED pattern. This can be clearly seen in Fig. 2(a) from the sharp 1×1 LEED image of a La-doped BaSnO₃ film. In contrast, we observe a 2×1 RHEED pattern, with the 2× reconstruction along the [110] azimuth of BaSnO₃ when the film growth conditions become slightly Ba-rich and move toward the boundary between region **III** and region **II** by either (1) increasing the substrate temperature, (2) lowering the flux supplied from the SnO₂ source, or (3) lowering the ozone partial pressure. Exiting region **III** and moving into region **II** is manifested by a more diffuse RHEED pattern with spots corresponding to the growth of a disordered Ruddlesden-Popper phase,⁶⁰⁻⁶² loaded with syntactic intergrowths of Ba_{n+1}Sn_nO_{3n+1} layers with varying *n*. The θ -2 θ XRD pattern of a sample film grown in region **II** exhibiting such intergrowth disorder is shown in the supplementary material (Fig. S2). This pattern can be indexed as Ba₈Sn₇O₂₂. A hallmark of intergrowth disorder is the presence of both even and odd XRD indices;^{63,64} an ideally ordered Ruddlesden-Popper phase would contain only even XRD indices because of the presence of the glide plane perpendicular to the *c*-axis.

If, on the other hand, starting from region **III** the fluxes are made more Sn-rich or the substrate temperature is lowered, a transmission RHEED pattern indicative of rough, three-dimensional growth is observed along both the [110] and [100] azimuths of BaSnO₃. This is indicative of the accumulation of SnO₂ in the film as the growth moves into region **IV**. The rough SnO₂ phase gives rise to the spots in the resulting RHEED pattern; the streaks are from the perovskite BaSnO₃ phase. The resulting mixed-phase sample corresponds to SnO₂+BaSnO₃ as shown by the XRD and RHEED results in the supplementary material (Fig. S5). Alternatively, if

one again starts in region **III** and increases the ozone pressure (leaving all other growth parameters constant) a three-dimensional transmission RHEED pattern indicative of condensed SnO₂ on the film surface is seen. All of these observed changes are fully consistent with the expectations implied by Fig. 1. The ability to see them *in situ* by RHEED allows one to reliably find the desired growth window (region **III**) for the adsorption-controlled growth of phase-pure BaSnO₃ thin films. For additional details see the supplementary material (S3).

Figure 2(b) shows RHEED intensity oscillations during the initial growth of a BaSnO₃ film on a (001) DyScO₃ substrate. The corresponding RHEED patterns of the same BaSnO₃ film along the [110] and [100] azimuths of BaSnO₃ are shown in Figs. 2(c) and 2(d), respectively. The RHEED intensity oscillation was monitored at the off-specular position (marked by the red box) along the [110] azimuth of BaSnO₃ shown in Fig. 2(c). Initially the BaSnO₃ film grew in a layer-by-layer growth mode, but due to the large lattice mismatch (−4.2%) between the (001) DyScO₃ substrate ($a_{\text{DyScO}_3, \text{pseudocubic}} = \sqrt{\frac{ab}{2}} = 3.943 \text{ \AA}$)⁶⁵ and BaSnO₃ film ($a_{\text{BaSnO}_3} = 4.116 \text{ \AA}$),⁶⁶ the film quickly relaxed and the amplitude of the RHEED oscillations decreased. Concomitant with this relaxation, the growth mode changed to step-flow after the growth of about 13-15 unit cells. The film growth rate was 0.3 Å/s (equivalently ~0.1 μm/hr), based on both the RHEED intensity oscillations and thickness fringes observed by XRD.

The same BaSnO₃ film characterized by RHEED in Figs. 2(b)-2(d)—a 60 nm thick La-doped BaSnO₃ film with a mobile carrier concentration of $1.2 \times 10^{20} \text{ cm}^{-3}$ grown on a 330 nm thick undoped BaSnO₃ buffer layer on a (001) DyScO₃ substrate—is characterized by XRD in Fig. 3. The θ -2 θ scan is shown in Fig. 3(a). The total film thickness is calculated based on the Kiessig fringes⁶⁷ around the 002 Bragg peak of the BaSnO₃, as shown in Fig. 3(b). The θ -2 θ scan exhibits solely the 00ℓ reflections of BaSnO₃ without any impurity phase. From these reflections

the c -axis of this La-doped BaSnO₃ film is calculated to be $c = 4.116 \pm 0.001 \text{ \AA}$ using a Nelson-Riley fit;⁶⁸ this is in agreement with the bulk lattice constant of BaSnO₃, $a = 4.116 \text{ \AA}$.⁶⁶ A comparison of the structural perfection of this same La-doped BaSnO₃ film and the underlying DyScO₃ substrate it was grown upon are shown in Fig. 3(c). Here, the rocking curve of the 002 peak of the La-doped BaSnO₃ film is overlaid upon the 004 peak of the DyScO₃ substrate. The full width at half maximum (FWHM) of the film peak is 0.016° , which is far broader than the 0.0062° FWHM of the substrate. Although narrower than all prior reported FWHM for as-grown BaSnO₃-based heterostructures,^{3,19,20,23,24} this relatively broad rocking curve is consistent with structural relaxation by the introduction of dislocations during the growth of the thick and highly mismatched (-4.2%) La-doped BaSnO₃ film on (001) DyScO₃. A reciprocal space map of the 103 BaSnO₃ peak of this same film is shown in Fig. 3(d). The in-plane and out-of-plane lattice constants of this La-doped BaSnO₃ film were calculated to be $4.1161 \pm 0.001 \text{ \AA}$ and $4.1163 \pm 0.001 \text{ \AA}$, respectively, indicating that the La-doped BaSnO₃ film is fully relaxed. An atomic force microscope image of this same film is shown in the supplementary material (S4).

Figure 4 shows the temperature dependence of (a) resistivity, (b) carrier concentration, and (c) mobility of the same La-doped BaSnO₃ sample characterized in Figs. 2(b)-2(d) and 3. The resistivity at room temperature is $2.3 \times 10^{-4} \text{ \Omega}\cdot\text{cm}$ and its temperature dependence exhibits metallic behavior down to 10 K with a resistivity ratio, $\rho_{300 \text{ K}} / \rho_{10 \text{ K}}$, of 2.15. The concentration of negatively charged mobile carriers (n) is temperature independent, as shown in Fig. 4(b). Assuming that all of the mobile carriers are attributable to the 60-nm-thick La-doped BaSnO₃ layer, the Hall resistance implies that n is $1.2 \times 10^{20} \text{ cm}^{-3}$. The mobility (μ) of this same sample was $183 \text{ cm}^2 \cdot \text{V}^{-1} \cdot \text{s}^{-1}$ at room temperature and reached $400 \text{ cm}^2 \cdot \text{V}^{-1} \cdot \text{s}^{-1}$ at 10 K as can be seen in

Fig. 4(c). This room-temperature mobility is 20% higher than the previous record, $150 \text{ cm}^2 \cdot \text{V}^{-1} \cdot \text{s}^{-1}$, which was achieved on a (110) PrScO_3 substrate.²²

The sample described in detail so far, is our highest mobility sample. The room-temperature mobility of other La-doped BaSnO_3 samples grown using the same adsorption-controlled growth conditions on a variety of substrates and with differing doping concentrations are shown in Fig. 4(d). These substrates ranged from SrTiO_3 to PrScO_3 , with lattice matches to BaSnO_3 ranging from -5.1% to -2.3% , respectively. Note that the room-temperature mobility of La-doped BaSnO_3 films on all of these substrates was higher than $160 \text{ cm}^2 \cdot \text{V}^{-1} \cdot \text{s}^{-1}$ for doping concentrations in the $(2-30) \times 10^{19} \text{ cm}^{-3}$ range. Additionally, our growth conditions enable films with mobile carrier concentrations all the way down to $1 \times 10^{18} \text{ cm}^{-3}$ to be achieved,⁶⁹ this is an order of magnitude lower than prior reports.^{2,3,19-24} The ability to dope BaSnO_3 at lower levels is consistent with the improved stoichiometry control that can accompany adsorption-controlled growth, leading to a reduction in the concentration of traps.

We investigated the defect structure of the La-doped BaSnO_3 sample with the highest mobility, the same sample whose other characteristics appear in Figs. 2-4, by STEM. A cross-sectional LAADF-STEM image of the entire film thickness is shown in Fig. 5(a). The high sensitivity of LAADF to strain and dislocations⁷⁰ makes it easy to see the threading dislocations. They are the vertically running defects with dark contrast in the BaSnO_3 film; one is indicated by a yellow arrow on Fig. 5(a). The HAADF-STEM images in Figs. 5(b) and 5(c) characterize the fully relaxed interface between the DyScO_3 substrate and the BaSnO_3 film. The spacing between the edge dislocations is on average 23 unit cells of DyScO_3 vs. 22 unit cells BaSnO_3 , which is consistent with that calculated from the ratio of the relaxed lattice parameters. Extended dislocations can also be seen, as indicated by the yellow arrow in Fig. 5(b).

The density of threading dislocations in the same high-mobility sample characterized in Figs. 2-5 was determined by plan-view STEM measurements (Fig. 6) to be $1.2 \times 10^{11} \text{ cm}^{-2}$. A high-resolution HAADF-STEM image is shown in Fig. 6(d) showing two partial edge dislocations, each with Burgers vectors having in-plane projections of $\frac{1}{2} \mathbf{a} \langle 110 \rangle$. A full dislocation with a Burgers vector having an in-plane projection of $\mathbf{a} \langle 110 \rangle$ is shown in the supplementary material (S5).

Interestingly, some of these dislocations have hollow cores. Being devoid of atoms, the hollow cores appear black in the plan-view HAADF-STEM images in Fig. 6(d) and Fig. S7 of the supplementary material. The magnitude of the smallest Burgers vector having an energetically stable hollow core lies in the range $20\pi \frac{\gamma}{\mu}$ to $40\pi\sqrt{e} \frac{\gamma}{\mu}$ for isotropic materials according to Frank's approximate theory,⁷¹ where γ is the surface energy and μ is the shear modulus. Using the calculated value of the surface energy (1.5 J/m^2)⁷² and the measured value of the shear modulus (99.9 GPa)⁷³ of BaSnO_3 , Frank's estimate of the minimum magnitude of the Burgers vector for it to have a hollow core lies in the 9-30 Å range. The two neighboring dislocations with outlined Burgers circuits in Fig. 6(d) both have Burgers vectors with in-plane projections of $\frac{1}{2} \mathbf{a} \langle 110 \rangle$, i.e., a magnitude $\frac{a}{\sqrt{2}}$ or 2.91 Å, yet one is hollow and the other is not. This could be because the out-of-plane component of the Burgers vectors of these two dislocations are not identical; they could have mixed character rather than being pure edge dislocations. Another possibility is that the adsorption controlled growth conditions lead to excess SnO_x species on the film surface during growth, which acts as a flux that lowers γ .⁷¹ The amount that γ is lowered depends on the concentration of flux and could vary spatially, leading to dislocations that are hollow or not hollow even though they have identical magnitudes of their Burgers vectors.

The huge density of dislocations observed in this film with record mobility ($1.2 \times 10^{11} \text{ cm}^{-2}$) led us to question if there might be some other defects besides dislocations that currently limit mobility in BaSnO_3 films. After all, our films are grown on the same substrates and have comparable dislocation densities to prior studies,¹⁹ yet the mobilities are far higher. How is it that our films have higher mobility? We do not know the answer to this question and are studying it further; what little we do know is mentioned below.

A potential culprit is Ruddlesden-Popper⁶⁰⁻⁶² $(\text{BaO})_2$ crystallographic shear defects, which have been reported to be a dominant structural defect in La-doped BaSnO_3 films grown by pulsed-laser deposition.⁷⁴ The TEM images in the study of Wang *et al.*⁷⁴ reveal a concentration of $(\text{BaO})_2$ crystallographic shear defects of about $2 \times 10^{11} \text{ cm}^{-2}$. In contrast, we see far fewer. We observed only one loop-shaped stacking fault in our highest mobility film (see the supplementary material (S6)). No stacking faults were observed in another two different areas with similar fields of view, leading us to estimate that the density of loop-shaped stacking faults in the film studied in Figs. 2-6 is about $3 \times 10^9 \text{ cm}^{-2}$.

Differences in point defect concentrations could also be responsible for our films exhibiting higher mobility than other BaSnO_3 films with comparable dislocation densities. Vacancies on the barium site (V''_{Ba}) or on the tin site (V''''_{Sn}) are low-energy acceptor defects^{75,76} in BaSnO_3 that could be responsible for the lack of conductivity in lightly La-doped BaSnO_3 films as well as the reduction in mobility when sufficient La is added to achieve conductivity. The local and automatic composition control provided by thermodynamics under adsorption-controlled growth conditions, could significantly reduce the concentration of V''_{Ba} , V''''_{Sn} , and other point defects, thus enhancing mobility. Note that adsorption-control is not synonymous with perfect composition control. Adsorption-control accesses the single-phase region of BaSnO_3 , but

depending on how wide that region is and from which side it is approached (in our case the SnO_x -rich side)—things that change with temperature and chemical potentials—the stoichiometry of the resulting film will change though it will always remain single phase. This is fully analogous to the growth of III-V compounds, where this behavior is well understood and utilized to controllably alter point defect concentrations, e.g., the EL2 defect in GaAs.⁷⁷

In summary, using adsorption-controlled MBE growth, La-doped BaSnO_3 thin films with room-temperature mobilities as high as $183 \text{ cm}^2 \cdot \text{V}^{-1} \cdot \text{s}^{-1}$ were achieved on highly mismatched substrates, despite high concentrations ($\sim 10^{11} \text{ cm}^{-2}$) of threading dislocations. Further, this growth method enabled La-doped BaSnO_3 with mobile carrier concentrations as low as $1 \times 10^{18} \text{ cm}^{-3}$ to be achieved.⁶⁹ These results imply that threading dislocations are not the only defects that have been limiting the mobility and trapping carriers in La-doped BaSnO_3 thin films. Other defects, possibly $(\text{BaO})_2$ crystallographic shear defects or point defects arising from non-stoichiometry, are potential culprits. These results make us believe that the combination of adsorption-controlled MBE with lattice-matched perovskite substrates will be a promising path to high-mobility La-doped BaSnO_3 thin films.

See supplementary material for additional details regarding the thermodynamic calculations as well as the structural and spectroscopic characterization of the BaSnO_3 films.

We gratefully acknowledge stimulating discussions with Karthik Krishnaswamy and Chris Van de Walle. This material is based upon work supported by the Air Force Office of Scientific Research under award number FA9550-16-1-0192 and by the National Science Foundation (Platform for the Accelerated Realization, Analysis, and Discovery of Interface Materials (PARADIM)) under Cooperative Agreement No. DMR-1539918. We also acknowledge support from the Center for Low Energy Systems Technology (LEAST), one of the six SRC STARnet

Centers, sponsored by MARCO and DARPA. This work made use of the Cornell Center for Materials Research (CCMR) Shared Facilities, which are supported through the NSF MRSEC program (DMR-1120296). Substrate preparation was performed in part at the Cornell NanoScale Facility, a member of the National Nanotechnology Coordinated Infrastructure (NNCI), which is supported by the NSF (Grant ECCS-15420819).

References

1. H. Hosono, *Thin Solid Films* **515**, 6000–6014 (2007).
2. H. J. Kim, U. Kim, H. M. Kim, T. H. Kim, H. S. Mun, B.-G. Jeon, K. T. Hong, W.-J. Lee, C. Ju, K. H. Kim, and K. Char, *Appl. Phys. Express.* **5**, 061102 (2012).
3. Useong Kim, *BaSnO₃: Thin Film Growth, Transport Properties, Devices, and Interfaces*, Ph.D. thesis, (Seoul National University, 2015) p. 15.
4. E. Sachet, C. T. Shelton, J. S. Harris, B. E. Gaddy, D. L. Irving, S. Curtarolo, B. F. Donovan, P. E. Hopkins, P. A. Sharma, A. L. Sharma, J. Ihlefeld, S. Franzen, and J.-P. Maria, *Nat. Mater.* **14**, 414–420 (2015).
5. Y. R. Wu and J. Singh, *IEEE Trans. Electron Devices* **52**, 284–293 (2005).
6. D. H. Looney, U.S. Patent No. 2,791,758 (May 7, 1957).
7. W. L. Brown, U.S. Patent No. 2,791,759 (May 7, 1957).
8. I. M. Ross, U.S. Patent No. 2,791,760 (May 7, 1957).
9. J. A. Morton, U.S. Patent No. 2,791,761 (May 7, 1957).
10. J. L. Moll and Y. Tarui, *IEEE Trans. Electron Devices* **10**, 338–339 (1963).
11. P. M. Heyman and G. H. Heilmeier, *Proc. IEEE* **54**, 842–848 (1966).
12. G. G. Teather and L. Young, *Solid State Electron.* **11**, 527–533 (1968).
13. L. L. Chang and L. Esaki, *IBM Tech. Discl. Bull.* **14**, 1250–1251 (1971).
14. S. Y. Wu, *IEEE Trans. Electron Devices* **21**, 499–504 (1974).
15. S. L. Miller and P. J. McWhorter, *J. Appl. Phys.* **72**, 5999–6010 (1992).
16. T. P. Ma and J.-P. Han, *IEEE Electron Device Lett.* **23**, 386–388 (2002).
17. S. Salahuddin and S. Datta, *Nano Lett.* **8**, 405–410 (2008).

18. A. I. Khan, K. Chatterjee, B. Wang, S. Drapcho, L. You, C. Serrao, S. R. Bakaul, R. Ramesh, and S. Salahuddin, *Nat. Mater.* **14**, 182–186 (2014).
19. H. Mun, U. Kim, H. Min Kim, C. Park, T. Hoon Kim, H. Joon Kim, K. Hoon Kim, and K. Char, *Appl. Phys. Lett.* **102**, 252105 (2013).
20. U. Kim, C. Park, T. Ha, R. Kim, H. S. Mun, H. M. Kim, H. J. Kim, T. H. Kim, N. Kim, J. Yu, K. H. Kim, J. H. Kim, and K. Char, *APL Mater.* **2**, 056107 (2014).
21. J. Shiogai, K. Nishihara, K. Sato, and A. Tsukazaki, *AIP Adv.* **6**, 065305 (2016).
22. S. Raghavan, T. Schumann, H. Kim, J. Y. Zhang, T. A. Cain, and S. Stemmer, *APL Mater.* **4**, 016106 (2016).
23. A. Prakash, P. Xu, A. Faghaninia, S. Shukla, J. W. Ager, C. S. Lo, and B. Jalan, *Nat. Commun.* **8**, 15167 (2017).
24. H. J. Kim, U. Kim, T. H. Kim, J. Kim, H. M. Kim, B.-G. Jeon, W.-J. Lee, H. S. Mun, K. T. Hong, J. Yu, K. Char, and K. H. Kim, *Phys. Rev. B* **86**, 165205 (2012).
25. Z. Galazka, R. Uecker, K. Irscher, D. Klimm, R. Bertram, A. Kwasniewski, M. Naumann, R. Schewski, M. Pietsch, U. Juda, A. Fiedler, M. Albrecht, S. Ganschow, T. Markurt, C. Guguschev, and M. Bickermann, *J. Phys.: Condens. Matter* **29**, 075701 (2017).
26. B. Pödör, *Phys. Status Solidi B* **16**, K167–K170 (1966).
27. D. Zhao and K. J. Kuhn, *IEEE Trans. Electron Devices* **38**, 2582–2589 (1991).
28. R. J. Egan, V. W. L. Chin, and T. L. Tansley, *J. Appl. Phys.* **75**, 2473–2476 (1994).
29. R. M. Feenstra and M. A. Lutz, *J. Appl. Phys.* **78**, 6091–6097 (1995).
30. H. M. Ng, D. Doppalapudi, T. D. Moustakas, N. G. Weimann, and L. F. Eastman, *Appl. Phys. Lett.* **73**, 821–823 (1998).

31. M. E. Klausmeier-Brown, J. N. Eckstein, I. Bozovic, and G. F. Virshup, *Appl. Phys. Lett.* **60**, 657–659 (1992).
32. S. J. Benerofe, C. H. Ahn, M. M. Wang, K. E. Kihlstrom, K. B. Do, S. B. Arnason, M. M. Fejer, T. H. Geballe, M. R. Beasley, and R. H. Hammond, *J. Vac. Sci. Technol. B* **12**, 1217–1220 (1994).
33. C. Lu and Y. Guan, *J. Vac. Sci. Technol. A* **13**, 1797–1801 (1995).
34. W. Wang, R. H. Hammond, M. M. Fejer, C. H. Ahn, M. R. Beasley, M. D. Levenson, and M. L. Bortz, *Appl. Phys. Lett.* **67**, 1375–1377 (1995).
35. B. Utz, S. Rieder-Zecha, and H. Kinder, *IEEE Trans. Appl. Supercond.* **7**, 1181–1184 (1997).
36. W. Wang, R. H. Hammond, M. M. Fejer, and M. R. Beasley, *J. Vac. Sci. Technol. A* **17**, 2676–2684 (1999).
37. J. H. Haeni, C. D. Theis, and D. G. Schlom, *J. Electroceram.* **4**, 385–391 (2000).
38. Y. Du, T. C. Droubay, A. V. Liyu, G. Li, and S. A. Chambers, *Appl. Phys. Lett.* **104**, 163110 (2014).
39. Y. Du and S. A. Chambers, *Appl. Phys. Lett.* **105**, 163113 (2014).
40. K. G. Günther, *Naturwissenschaften* **45**, 415–416 (1958).
41. J. R. Arthur, Jr., *J. Appl. Phys.* **39**, 4032–4034 (1968).
42. A. Y. Cho, *Surf. Sci.* **17**, 494–503 (1969).
43. A. Y. Cho, *J. Appl. Phys.* **41**, 2780–2786 (1970).
44. A. Y. Cho, *J. Appl. Phys.* **42**, 2074–2081 (1971).
45. H. Freller and K. G. Günther, *Thin Solid Films* **88**, 291–307 (1982).
46. R. Heckingbottom, G. J. Davies, and K. A. Prior, *Surf. Sci.* **132**, 375–389 (1983).

47. H. Seki and A. Koukitu, *J. Cryst. Growth* **78**, 342–352 (1986).
48. J. Y. Tsao, *J. Cryst. Growth* **110**, 595–603 (1991).
49. J. Y. Tsao, *Materials Fundamentals of Molecular Beam Epitaxy* (Academic Press, Boston, 1993) pp. 65–88.
50. G. Dormans, P. J. Van Veldhoven, and M. de Keijser, *J. Cryst. Growth* **123** (1992) 537–544.
51. C. D. Theis and D. G. Schlom, *J. Cryst. Growth* **174**, 473–479 (1997).
52. E. H. Smith, J. F. Ihlefeld, C. A. Heikes, H. Paik, Y. Nie, C. Adamo, T. Heeg, Z. K. Liu, and D. G. Schlom, *Phys. Rev. Mater.* **1**, 023403 (2017)
53. A. Prakash, P. Xu, X. Wu, G. Haugstad, X. Wang, and B. Jalan, *J. Mater. Chem. C* **5**, 5730–5736 (2017).
54. MKS ASTeX model AX8401 ozone generator, MKS Instruments, Wilmington, MA, U.S.A.
55. R. E. Honig and D. A. Kramer, *RCA Rev.* **30**, 285–305 (1969).
56. R. H. Lamoreaux, D. L. Hildenbrand, and L. Brewer, *J. Phys. Chem. Ref. Data* **16**, 419–443 (1987).
57. R. Uecker, D. Klimm, R. Bertram, M. Bernhagen, I. Schulze-Jonack, M. Brützam, A. Kwasniewski, T. M. Gesing, and D. G. Schlom, *Acta Phys. Pol., A* **124**, 295–300 (2013).
58. Z.-K. Liu, *J. Phase Equilib. Diffus.* **30**, 517–534 (2009).
59. Y. Li, L. Zhang, Y. Ma, and D. J. Singh, *APL Mater.* **3**, 011102 (2015).
60. D. Balz and K. Plieth, *Z. Elektrochem.* **59**, 545–551 (1955).
61. S.N. Ruddlesden and P. Popper, *Acta Cryst.* **10**, 538–539 (1957).
62. S.N. Ruddlesden and P. Popper, *Acta Cryst.* **11**, 54–55 (1958).

63. R. Takahashi, K. Valset, E. Folven, E. Eberg, J. K. Grepstad, and T. Tybell, *Appl. Phys. Lett.* **97**, 081906 (2010).
64. C. M. Brooks, L. Fitting Kourkoutis, T. Heeg, J. Schubert, D. A. Muller, and D. G. Schlom, *Appl. Phys Lett.* **94**, 162905 (2009).
65. R. Uecker, B. Velickov, D. Klimm, R. Bertram, M. Bernhagen, M. Rabe, M. Albrecht, R. Fornari, and D. G. Schlom, *J. Cryst. Growth* **310**, 2649–2658 (2008).
66. F. G. Kinyanjui, S. T. Norberg, C. S. Knee, I. Ahmed, S. Hull, L. Buannic, I. Hung, Z. Gan, F. Blanc, C. P. Grey, and S. G. Eriksson, *J. Mater. Chem. A* **4**, 5088–5101 (2016).
67. H. Kiessig, *Ann. Phys.* **402**, 769–788 (1931).
68. J. B. Nelson and D. P. Riley, *Proc. Phys. Soc., London* **57**, 160–177 (1945).
69. J. Park, N. Tanen, H. Paik, D. Jena, and D. G. Schlom (unpublished).
70. D. A. Muller, N. Nakagawa, A. Ohtomo, J. L. Grazul, and H. Y. Hwang, *Nature* **430**, 657–661 (2004).
71. F. C. Frank, *Acta Cryst.* **4**, 497–501 (1951).
72. A. Slassi, M. Hammi, and O. El Rhazouani, *J. Electron. Mater.* **46**, 4133–4139 (2017).
73. T. Maekawa, K. Kurosaki, and S. Yamanaka, *J. Alloys Compd.* **416**, 214–217 (2006).
74. W. Y. Wang, Y. L. Tang, Y. L. Zhu, J. Suriyaprakash, Y. B. Xu, Y. Liu, B. Gao, S. W. Cheong, and X. L. Ma, *Sci. Rep.* **5**, 16097 (2015).
75. D. O. Scanlon, *Phys. Rev. B* **87**, 161201 (2013).
76. L. Weston, L. Bjaalie, K. Krishnaswamy, and C. G. Van de Walle (unpublished).
77. D. T. J. Hurle, *J. Appl. Phys.* **107**, 121301 (2010).

Table I. Reaction enthalpy (ΔH) values for the formation of $\text{Ba}_{n+1}\text{Sn}_n\text{O}_{3n+1}$ phases with $n=1, 2, 3,$ and 4, calculated from first-principles with the PBEsol functional.

| Reaction | ΔH (eV/atom) | ΔH (kJ/mol-f.u.) |
|---------------------------------------------------------------------|----------------------|--------------------------|
| $\text{BaO} + \text{SnO}_2 = \text{BaSnO}_3$ | -0.223 | -107.5 |
| $2\text{BaO} + \text{SnO}_2 = \text{Ba}_2\text{SnO}_4$ | -0.228 | -154.2 |
| $3\text{BaO} + 2\text{SnO}_2 = \text{Ba}_3\text{Sn}_2\text{O}_7$ | -0.227 | -262.4 |
| $4\text{BaO} + 3\text{SnO}_2 = \text{Ba}_4\text{Sn}_3\text{O}_{10}$ | -0.225 | -369.3 |

Figure 1. Calculated Ellingham diagram (oxygen partial pressure vs. reciprocal temperature with the tin partial pressure fixed at 7.6×10^{-8} Torr (10^{-10} atm) assuming an open system. The overlaid RHEED patterns are taken along the [110] BaSnO_3 azimuth from films grown on (001) DyScO_3 substrates at different substrate temperatures. The four regions of phase stability between SnO_x gases and the condensed phases are represented as **(I)** BaO , **(II)** Ba_2SnO_4 , **(III)** BaSnO_3 , and **(IV)** SnO_2 , respectively, where the name of each region corresponds to the major condensed phase present. First-principles calculations, using the generalized gradient approximation (GGA) with Perdew–Burke–Ernzerhof revised for solids (PBEsol) functional, predicted the enthalpy of BaSnO_3 formation to be -107.5 kJ/mol per formula unit for the $\text{BaO} + \text{SnO}_2 = \text{BaSnO}_3$ reaction (see Table I).

Figure 2. (a) Low-energy electron diffraction (LEED) pattern of a 25 nm thick, 3.5 at. % La-doped BaSnO_3 thin film grown on a (110) TbScO_3 substrate. (b) Reflection high-energy electron diffraction (RHEED) intensity oscillation during the growth of an undoped BaSnO_3 buffer layer

on a (001) DyScO₃ substrate. RHEED images of a 60 nm thick La-doped BaSnO₃ film with a mobile carrier concentration of $1.2 \times 10^{20} \text{ cm}^{-3}$ (grown on top of the 330 nm thick undoped BaSnO₃ buffer layer shown in (b)) viewed along the (c) [110] and (d) [100] azimuth of BaSnO₃.

Figure 3. XRD scans of a 60 nm thick La-doped BaSnO₃ film grown on a 330 nm thick undoped BaSnO₃ buffered layer on a (001) DyScO₃ substrate measured in a triple-axis geometry. (a) θ - 2θ scan. (b) A close-up view of the θ - 2θ scan around the 002 La-doped BaSnO₃ peak showing clear thickness fringes. The total thickness of the BaSnO₃ film is calculated to be 390 ± 0.2 nm. (c) Overlaid rocking curves of the 002 BaSnO₃ film peak and the 004 DyScO₃ substrate peak. (d) A reciprocal space map around the 103 BaSnO₃ film and the 332 DyScO₃ substrate peak. The substrate peaks are labeled with asterisks.

Figure 4. (a) Resistivity vs. temperature, (b) mobile electron carrier concentration vs. temperature, and (c) electron mobility vs. temperature of the same La-doped BaSnO₃ film characterized in Figs. 2(b)-2(d) and 3. In (d) measurements of the mobility vs. mobile electron carrier concentration are made for a multitude of La-doped BaSnO₃ films grown on (100) SrTiO₃, (001) DyScO₃, (110) DyScO₃, (110) TbScO₃, (110) GdScO₃, (110) Nd_{0.5}Sm_{0.5}ScO₃, (110) NdScO₃, and (110) PrScO₃ substrates. All of the “Cornell” films were grown under the adsorption-controlled growth conditions described. Also plotted for comparison are the highest mobility La-doped BaSnO₃ single crystals from Kim *et al.*² at Seoul National University (SNU, solid blue squares) and the highest mobility La-doped BaSnO₃ films from Raghavan *et al.*²² at the University of California, Santa Barbara (UCSB, green triangle),

Kim *et al.*^{2,24} at SNU (purple diamond), Shiogai *et al.*²¹ at Tohoku University (orange upside down triangle), and Prakash *et al.*²³ at the University of Minnesota (cyan sideways triangle).

Figure 5. Cross-sectional STEM images of the same La-doped BaSnO₃ film characterized in Figs. 2-4. (a) LAADF-STEM image showing the entire film thickness. The yellow arrow indicates a threading dislocation. HAADF-STEM images of the BaSnO₃/DyScO₃ interface are shown in (b) and (c). Edge dislocations are labeled on (c).

Figure 6. Plan-view STEM images of the same La-doped BaSnO₃ film characterized in Figs. 2-5. (a) Bright-field and (b) dark-field STEM images. (c) and (d) are low and high magnification HAADF-STEM images, respectively. From these images the density of threading dislocations is $1.2 \times 10^{11} \text{ cm}^{-2}$. The yellow arrow in (a) shows a threading dislocation. Four dislocations are present in (d). The Burgers circuit is drawn for the two on the left, revealing two partial edge dislocations, each with a Burgers vector with an in-plane projection of $\frac{1}{2} \mathbf{a} \langle 110 \rangle$. The dislocation that is arrowed is not hollow, whereas the dislocation below it is hollow.

Figure 1.

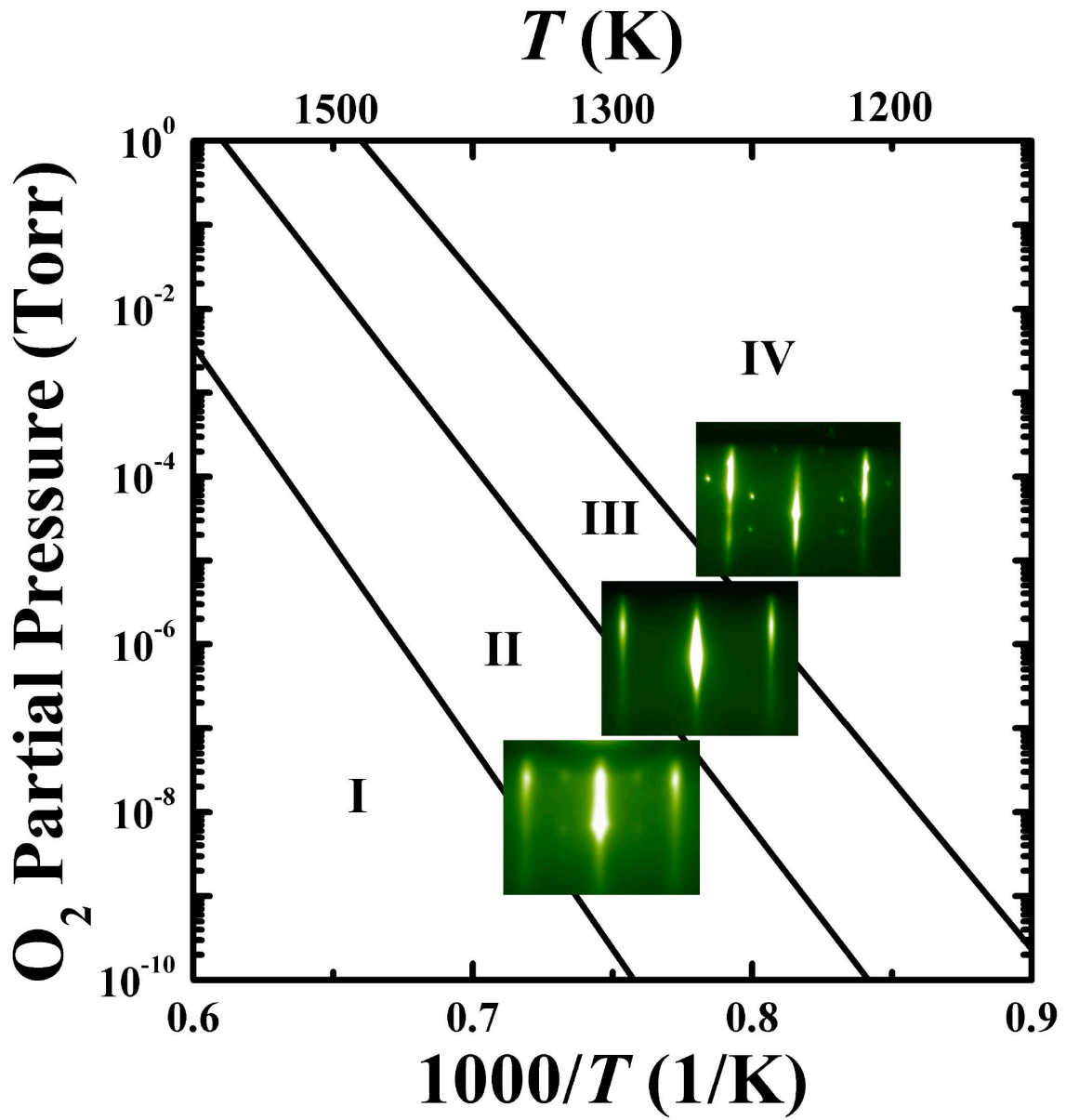


Figure 2.

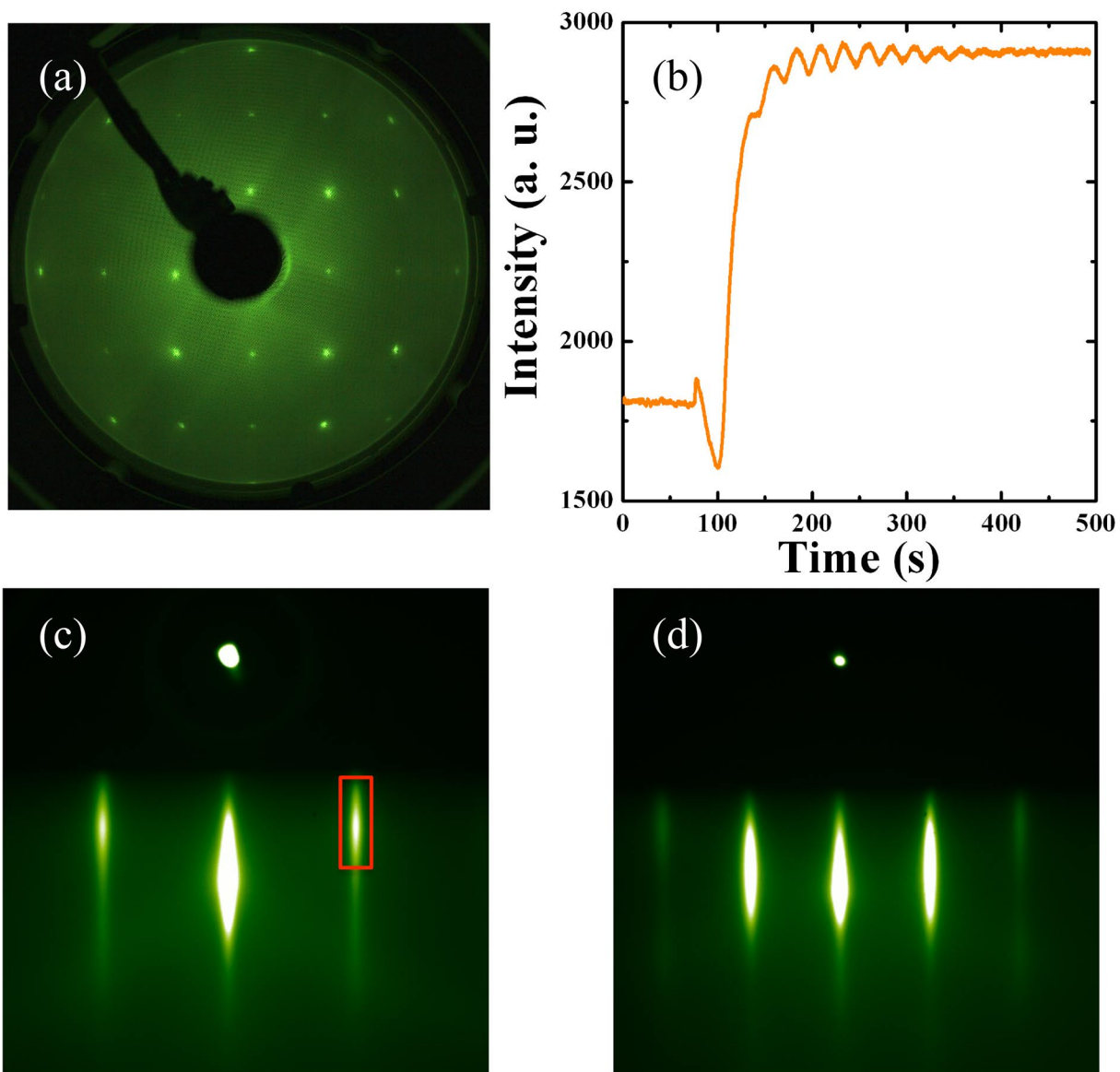


Figure 3.

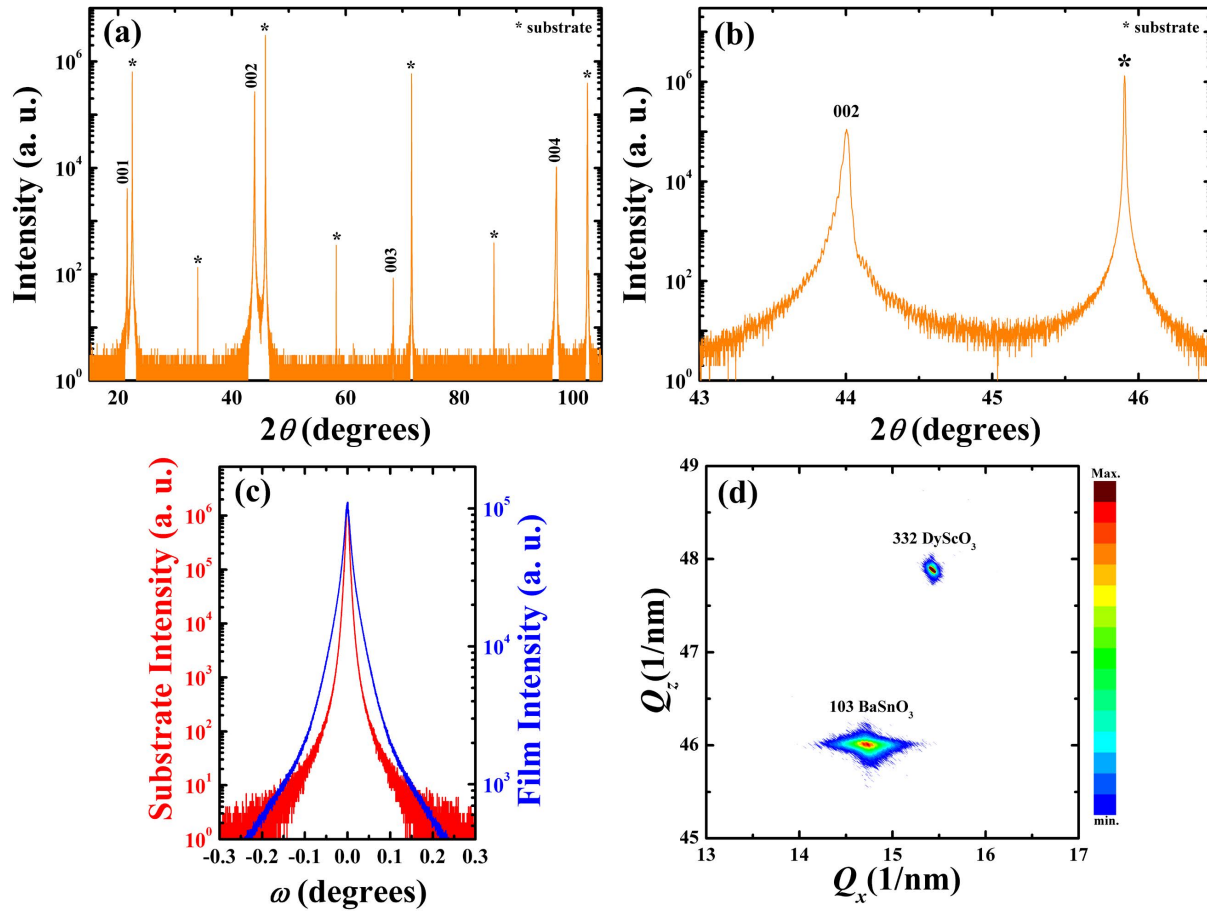


Figure 4.

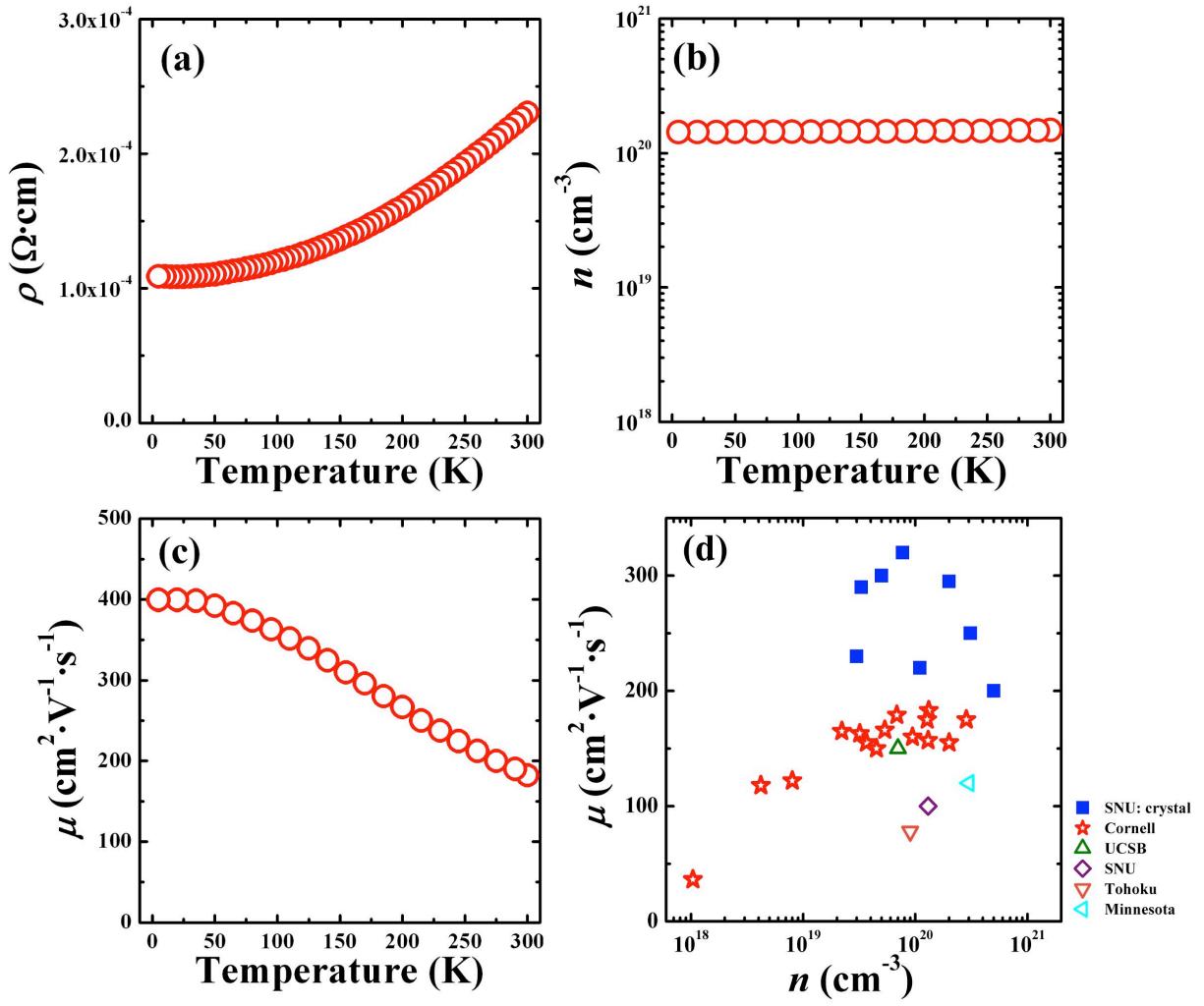


Figure 5.

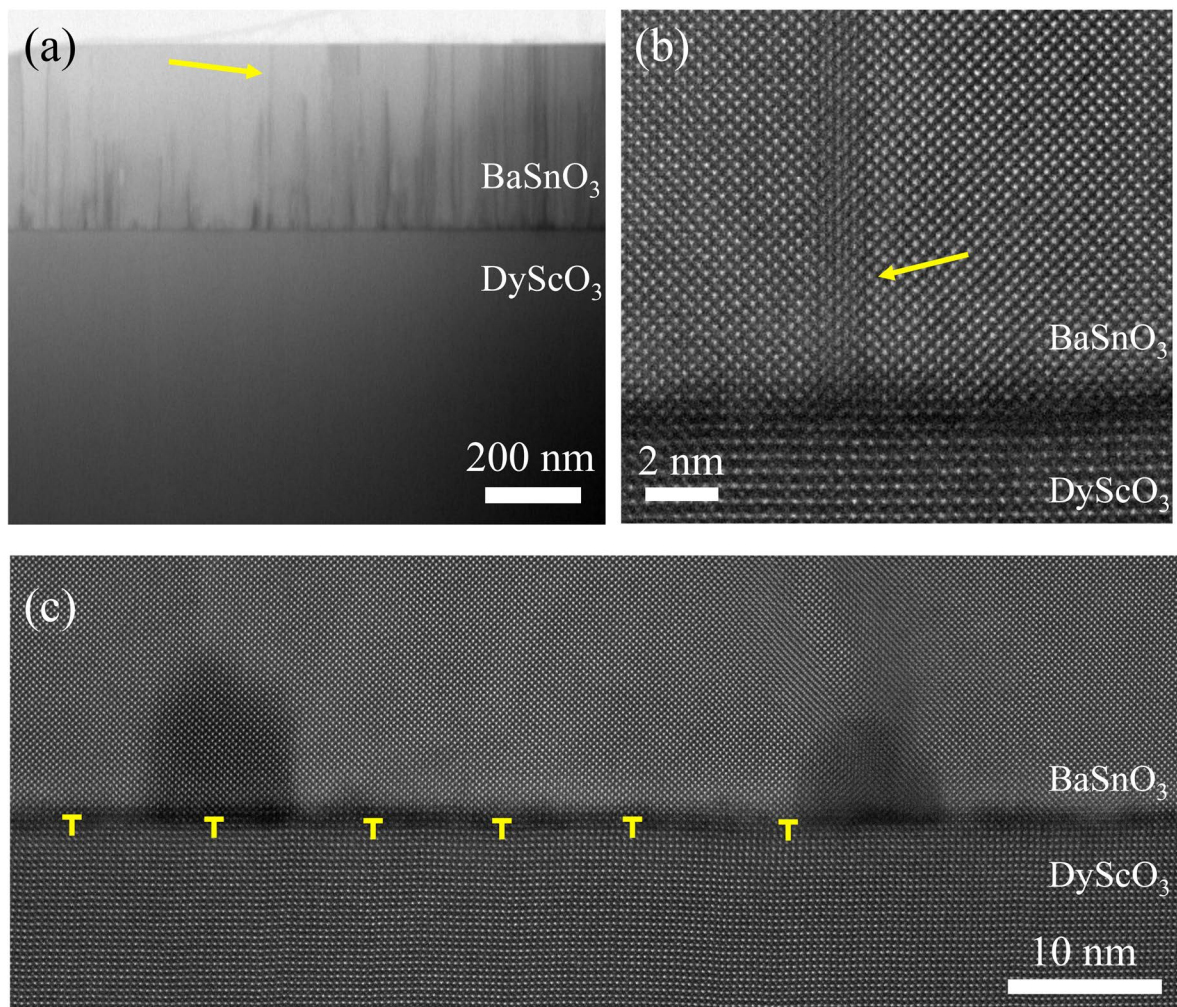


Figure 6.

